Automated detection of type 3 neovascularization biomarkers in age-related macular degeneration using OCT images and a complex direction field

Ravil Samigullin[1][0009-0009-1803-4907], Natalia Ilyasova[1, 2][0000-0003-3027-1963], Nikita Demin[1, 2][0000-0002-8707-770X], Evgeniy Zamytskiy[3][0000-0002-0258-165X], Andrey Zolotarev[3][0000-0002-9107-5221]

[1] Samara National Research University, Samara 443086, Russia
[2] Image Processing Systems Institute, NRC "Kurchatov Institute", Molodogvardeyskaya Street 151, 443001 Samara, Russia
[3] Samara State Medical University, Chapayevskaya Street 89, 443079 Samara, Russia
samigullin.ravil2015@yandex.ru

Abstract. This paper presents a method for identifying biomarkers of type III neovascularization in age-related macular degeneration (AMD) based on the analysis of the complex direction field of OCT images of the retina. The developed method includes the following sequential steps: constructing the retinal direction field, smoothing it using linear filtering, extracting quantitative diagnostic features (density of sharp transitions, relative area of distinct lines, number of heterogeneous regions, unidirectionality of retinal layers), and classifying images using a trained model. To optimize the method, a parameter selection was performed: the size of the direction field construction mask, the size of the filter mask, the number of filtering passes, and the threshold of the weighting function. The experimental study was conducted on a sample of 160 OCT images (80 normal, 80 pathological). It is shown that the developed method achieves accuracy = 0.97 and ROC AUC = 0.99 when using logistic regression as the classifier. The method has high reproducibility and can be integrated into an ophthalmologist's decision support system for the automated diagnosis of type III neovascularization in AMD.

Keywords: age-related macular degeneration, type III neovascularization, optical coherence tomography, direction fields, texture analysis, image classification, retinal biomarkers.

1 Introduction

Age-related macular degeneration (AMD) is one of the leading causes of irreversible vision loss in the elderly, with macular neovascularization (MNV) considered the most severe form of the disease [1, 2]. Among MNV subtypes, type 3 – also known as retinal angiomatous proliferation – attracts particular clinical interest. It is characterized by intraretinal origin of newly formed vessels and a specific pattern of disorganization of the layered retinal structure [5, 6]. Distinguishing type 3 MNV from types 1 and 2 has

prognostic value, because these subtypes differ in their response to anti-VEGF therapy, anatomical localization of the process, and progression rate [2, 3]. Nevertheless, during visual assessment of OCT images, type 3 is often misidentified due to partial overlap of morphological features with other subtypes, leading to diagnostic errors and treatment delay [4, 5]. Therefore, the development of objective quantitative tools for detecting biomarkers specific to type 3 MNV represents a relevant scientific and practical direction.

Modern ophthalmology actively uses optical coherence tomography (OCT), which provides detailed images of the neurosensory retina and retinal pigment epithelium (RPE) [1]. Key biomarkers of type 3 neovascularization include blurring of the boundaries between retinal layers, focal breaks, and areas with disrupted spatial orientation of tissues [6]. Manual recognition of such changes is time-consuming and suffers from inter-expert variability, which limits its adoption into routine clinical practice. In recent years, machine learning algorithms, especially convolutional neural network architectures (e.g., U-Net), have demonstrated high performance in segmenting retinal structures and pathological lesions on OCT [7–19].

In recent years, studies aimed at automated analysis of type 3 MNV have emerged. The study [5] used quantitative analysis of OCTA images to assess vascular differences between MNV types. Work [20] applied deep learning to predict the risk of neovascularization in the fellow eye based on structural OCT images. Study [11] developed a convolutional neural network for classifying MNV subtypes on OCT images. All of the above approaches are based on the analysis of morphological or vascular features using deep learning. In contrast, the method proposed in this paper is based on the analysis of a complex direction field, which allows quantitative assessment of retinal layer disorganization and, to the best of our knowledge, has not been previously used for detecting type 3 MNV.

In the present study, U-Net is used to automatically segment the pigment epithelium and the neurosensory retina, providing a basis for subsequent quantitative analysis.

Nevertheless, approaches based solely on segmentation do not always fully account for the textural and orientational characteristics of tissues. Yet these characteristics can serve as informative diagnostic features for differentiating neovascularization subtypes. For the analysis of quasi-periodic structures, such as retinal layers on OCT, the direction field is a promising tool [21–24]. This apparatus makes it possible to detect disruptions of structural regularity associated with pathology and is suitable for identifying type 3 MNV biomarkers.

The aim of this work is to develop and experimentally validate a method for identifying type 3 neovascularization biomarkers based on the analysis of a complex direction field of OCT retinal images. The proposed method includes sequential steps: calculation of the direction field, its smoothing, extraction of a set of quantitative diagnostic parameters, and subsequent image classification. Unlike many existing solutions focused on segmentation, our approach directly assesses the degree of order of the layered architecture and identifies zones of its disruption, which corresponds to the clinical picture of type 3 MNV.

2 Materials and Methods

2.1 Data Description

This study is based on a retrospective collection of OCT images of the macular region obtained from clinical tomographs. The original DICOM data were converted into PNG raster format while preserving the spatial resolution of 744×470 pixels per B-scan.

The dataset included images from patients with verified age-related macular degeneration (AMD), including cases of type 3 macular neovascularization (MNV). Data annotation was performed by expert ophthalmologists: for each B-scan, binary masks were created to isolate two anatomical structures – the neurosensory retina and the retinal pigment epithelium (RPE). The total volume of annotated data comprised 86 image–mask pairs.

To expand the training set, geometric augmentation methods – rotations and mirror reflections – were applied. As a result, the final dataset was increased to 172 pairs.

Both original OCT images (in grayscale) and their segmentation results were used in the work. Segmentation was performed using a convolutional neural network architecture U-Net trained on the described dataset. The obtained segmentation masks serve to define regions of interest (ROI), which allows subsequent analysis to be restricted to tissue structures and to exclude background artifacts. At the same time, the direction field analysis is performed directly on the original brightness images (without applying the mask), while the segmentation masks are used at the feature extraction stage for normalization and localization.

2.2 Theoretical Background: Direction Field (DF)

To quantitatively assess the orderliness of layered structures in OCT images, this work employs the concept of a direction field (DF). Each image point is assigned an angle that characterizes the predominant orientation of local textures in its neighborhood [24–26, 27]. In other words, this angle specifies the direction of the tangent to the brightness isophote. For OCT images, the direction field makes it possible to numerically describe the spatial distribution of tissue contours and textures.

A specific feature of the direction field is the periodicity of angles with a period of π, which complicates the application of standard statistical processing and linear filtering methods. To solve this problem, a complex representation of the direction field is used [27], in which the direction ψ and its reliability w are combined into a complex quantity.

$$\dot{\psi}(x_1, x_2) = w(x_1, x_2)\exp\left(i2\psi(x_1, x_2)\right) \tag{1}$$

The weight function ($w(x,y)$) characterizes the reliability of the direction estimate: in areas with pronounced structure, its value is close to unity, while in homogeneous regions it tends to zero. Such a representation allows smoothing and filtering of the direction field using standard linear methods.

To construct the direction field, this work uses the projection-dispersion method [27, 28], based on the analysis of the brightness distribution within a local image window. An illustration of the method is shown in Figure 1. The method employs the Radon transform [28] to determine the direction of greatest consistency of the local structure and is highly robust to noise.

In the discrete implementation, the image is scanned with a square mask of size $M \times M$. For each mask position and for each of four directions $\varphi = 0°, 45°, 90°, 135°$, brightness projections $R(k, \psi)$ – are computed – the mean values of samples along lines parallel to ψ. Then, for each direction, the variance of these projections is estimated using the discrete analog of the projection-dispersion method [27, 28]:

$$D(\psi) = \sum_k \xi(k,\psi)\left[R(k,\psi) - R(\psi)\right]^2, \; \bar{R}(\psi) = \sum_k \xi(k,\psi) R(k,\psi), \qquad (2)$$

where $\xi(k,\psi)$ – are weighting coefficients that depend on the projection length (for vertical and horizontal directions, $\xi = 1/M$, $k = 1, \ldots, M$). The direction corresponding to the minimum variance $D(\psi)$, is taken as the local direction of the textural structure.

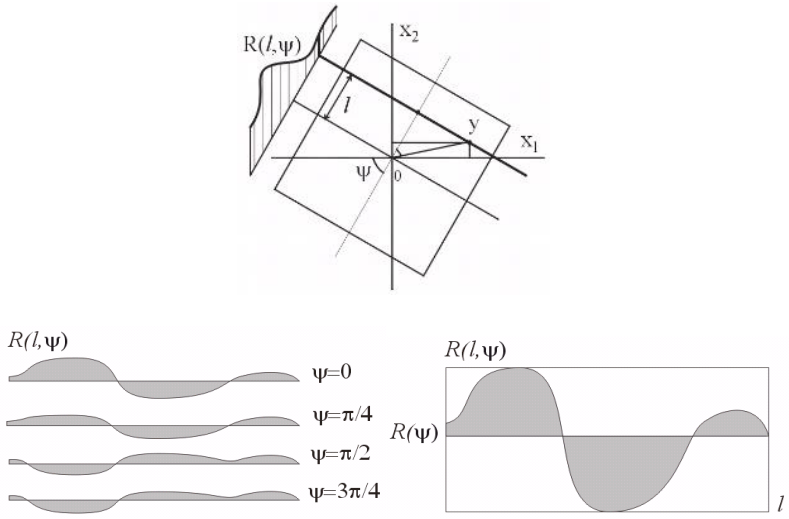

Fig. 1. – Illustration of the projection-dispersion method

2.3 Extraction of Diagnostic Features Based on the Direction Field

Automated analysis allows obtaining not only a qualitative but also a quantitative assessment of structural disturbances in the retinal layers. Based on the methodology of the Yeroshevsky Hospital physicians, which relies on the analysis of images a priori divided into normal and pathological (for type 3 neovascularization), classification features were identified that are based on geometric parameters of the structure under study. Figure 2 shows examples of direction fields (DF) for normal and pathological cases with different numbers of filtering passes.

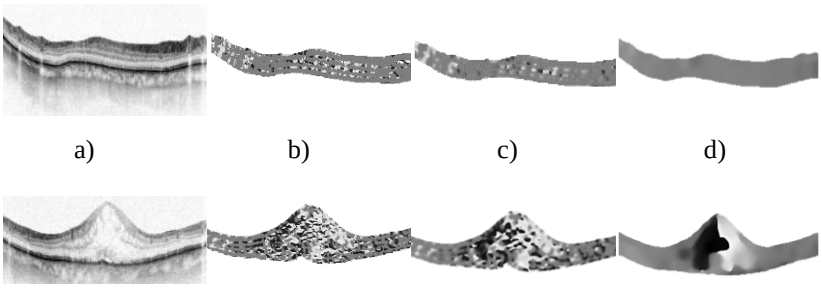

Fig. 2. – Direction fields (DF) for retinal OCT images (a–d – normal, e–h – pathology): a, e – brightness function of the original image; b, f – four-gradation DF, projection-dispersion method; c, g – linear smoothing of DF (11×11 window, 1 pass); d, h – linear smoothing of DF (11×11 window, 30 passes, threshold 0.4).

According to this methodology, normal retinal layers have clearly expressed near-horizontal directions and a uniform spatial structure. In a normal image (Fig. 2a–d): the original brightness pattern (a) shows horizontal layers; the four-gradation DF (b) is mostly homogeneous; after one smoothing pass (c) the direction field becomes smoother; after 30 passes (d) it is almost unidirectional without breaks. In pathology (Fig. 2e–h), layer mixing and breaks occur. The original image (e) contains disorganized tissue; the DF (f) has many differently oriented fragments; one smoothing pass (g) only partially reduces noise, while 30 passes (h) preserve and even highlight pathological inhomogeneities – consistent with type 3 neovascularization. Increasing the number of passes (compare Fig. 2c,g and Fig. 2d,h) improves DF homogeneity in normal areas but emphasises pathological changes. This increases separability of diagnostic features and classification accuracy. Several features enable classification: (a) unidirectionality of retinal layers, (b) relative area of regions with pronounced direction, (c) degree of directional smoothness within the mask, and (d) number of heterogeneous regions (local anisotropy). These characteristics are based on the direction field. A formal description of features K_1–K_4 is given below.

Criterion for the density of sharp directional transitions (K_1)

To quantitatively assess local changes in direction within the image, the spatial derivative of the angular direction field is used. To avoid ambiguity due to the periodicity of the angles, the directional gradient is first computed in vector form. For each pixel *(x,y)*, the local direction angle is denoted as $\theta(x,y)$. The gradient of the directionality magnitude $G(x,y)$ is then defined as:

$$G(x,y) = \sqrt{\left(\frac{\partial}{\partial x}\cos(\theta(x,y))\right)^2 + \left(\frac{\partial}{\partial x}\sin(\theta(x,y))\right)^2} \quad (3)$$

where $\theta(x,y) \in [0,\pi)$ is the direction angle at that point (in radians), cos(θ) and sin(θ) convert the direction into a vector representation on the unit circle, the partial derivatives with respect to x and y are approximated using finite differences, and $G(x,y)$ reflects the intensity of the local change in direction, analogous to the gradient magnitude in an image.

After obtaining the map $G(x,y)$, the coefficient K_1, is calculated, which characterizes the number of pixels where sharp local direction transitions occur. It is defined as:

$$K_1 = \sum_{(x,y)} G(x,y) > \tau \tag{4}$$

where τ is an empirically set threshold that separates weak direction changes from sharp ones (the value used in the implementation is provided). Thus, K_1 - represents the absolute number of points with a sharp change in direction and can serve as a marker of structural transitions.

Criterion for the relative area of regions with distinct lines (K_2)

In the image of the retinal layers (Figure 2), spatial heterogeneity is clearly observed: some regions are characterized by clear, well-distinguishable boundaries between layers, while others consist of blurred or unstructured areas, as well as zones with pronounced homogeneity (homogeneous patches). In the presence of pathological changes, such as neovascularization or layer destruction, the proportion of such unstructured regions generally increases. To quantitatively assess the prominence of structural lines, a weight function associated with the complex direction field is used. This function takes higher values in those image fragments where the layered structure is most distinct and the local directionality is formed stably. Based on experimental studies, a threshold value of the weight function was empirically established, allowing effective separation of regions with a clearly expressed linear structure from fragments characterized by blurring or lack of order.

The calculation algorithm is based on threshold binarization of the weight image obtained from the direction field analysis (Figure 2), which selects only those regions where the weight function values exceed a given threshold. To quantify the proportion of well-structured regions, a line clarity coefficient – a dimensionless parameter reflecting the relative area of such regions – is introduced:

$$K_2 = S_p / S \tag{5}$$

where S - is the area of the entire image, and S_p - is the total area of regions where the weight function value is not less than the threshold value.

Criterion for the number of heterogeneous regions (K_3)

The values of the function $\gamma(x_1, x_2)$, defined below (9) are normalized and then inverted:

$$\gamma_{inv} = 1 - \frac{\gamma - \gamma_{\min}}{\gamma_{\max} - \gamma_{\min} + \varepsilon} \tag{6}$$

Thus, high values of γ_{inv} correspond to smooth and stable structures, while low values correspond to potentially pathological, heterogeneous areas. The criterion K_3 is the number of "dark" pixels (low values of γ_{inv}), within the mask that do not pass the filtering threshold:

$$K_3 = \sum_{x,y} \gamma_{inv}(x,y) < T \tag{7}$$

The higher the value of K_3, the greater the proportion of heterogeneous, disrupted areas, which may indicate degenerative or inflammatory processes in the retina.

Criterion for the unidirectionality of retinal layers (K_4)

The criterion for the unidirectionality of retinal layers is shown in Figure 2. In the absence of pathological changes, the retinal layers are characterized by a clearly expressed unidirectionality, i.e., they have a small spread of directions.

In formalized form, this classification criterion is expressed by a unidirectionality parameter, which is computed based on the analysis of the filtered direction field of the retinal layer image. To detect jumps (contours) in the direction field, a quantity equal to the squared magnitude of the gradient of the complex direction field is used:

$$\gamma(x_1, x_2) = \left| \frac{\partial \dot{\psi}(x_1, x_2)}{\partial x_1} \right|^2 + \left| \frac{\partial \dot{\psi}(x_1, x_2)}{\partial x_2} \right|^2 \tag{8}$$

For a unit weight function, we obtain:

$$\begin{aligned} \gamma(x_1, x_2) = &\left(\frac{\partial \sin 2\psi(x_1, x_2)}{\partial x_1} \right)^2 + \left(\frac{\partial \sin 2\psi(x_1, x_2)}{\partial x_2} \right)^2 + \\ &+ \left(\frac{\partial \cos 2\psi(x_1, x_2)}{\partial x_1} \right)^2 + \left(\frac{\partial \cos 2\psi(x_1, x_2)}{\partial x_2} \right)^2 \end{aligned} \tag{9}$$

The unidirectionality coefficient is taken as the average value of $\gamma(x_1, x_2)$ over the image:

$$K_4 = \frac{1}{|D|} \iint_D \gamma(x_1, x_2) dx_1 dx_2 \tag{10}$$

The contour characteristic of the direction field corresponding to K_4, is shown in Figure 2. The value of K_4 is smaller when the layers are more unidirectional and increases when chaotic changes appear.

3 Results

3.1 Qualitative Analysis

Figure 3 shows the criterion for the unidirectionality of retinal layers. For the normal case (Fig. 3a–c), the original image (a) has smooth layers, the weight map (b) shows high values over extensive connected areas, and after binarization (c) a compact region corresponding to the regular structure is highlighted. In pathology (Fig. 3d–f), the original image (d) contains breaks and mixing of layers, the weight map (e) is fragmented, and binarization (f) reveals many small disconnected zones, indicating a loss of order.

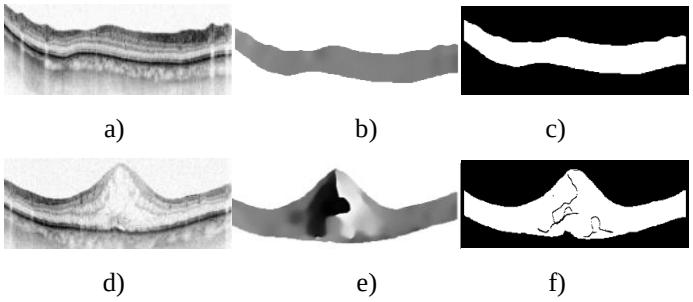

Fig. 3. – Unidirectionality criterion: original image (a, d), weight map (b, e) and its binarization (c, f) for normal (a–c) and pathology (d–f).

Figure 4 shows a visualization of the criterion for the relative area of regions with distinct lines (feature K2). For the normal case (Fig. 4a–c), the original image (a) has well-defined boundaries, filtering of the direction field (b) emphasizes their connectivity, and contour extraction (c) yields thin continuous lines. In pathology (Fig. 4d–f), the original image (d) is characterized by blurred structure, direction field filtering (e) produces broken and chaotic fragments, and the contour map (f) contains many disconnected short lines, indicating layer destruction.

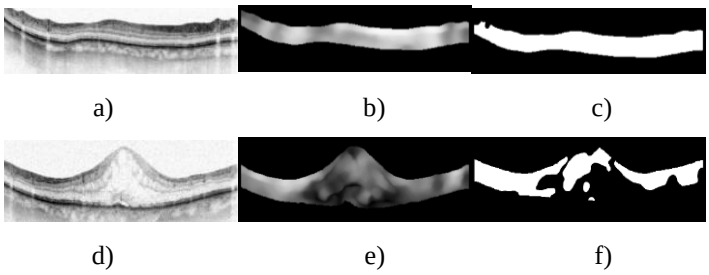

Fig. 4. - Criterion for the relative area of distinct lines: original image (a, d), direction field filtering (b, e), and contour extraction (c, f) for normal (a–c) and pathology (d–f).

Thus, the qualitative analysis confirms that the proposed method allows visual discrimination between normal and pathological images based on the structure of the direction field, the weight function, and the contour map.

3.2 Quantitative Assessment of Features

Table 1 presents typical examples of the diagnostic feature values K1 (density of sharp directional transitions), K2 (relative area of regions with distinct lines), K3 (number of heterogeneous regions), and K4 (degree of unidirectionality) for six retinal OCT images. Three correspond to normal, three to pathology (type 3 neovascularization in AMD). For each example, the original image, the direction field (DF), and the numerical feature values are provided.

Table 1. – Typical values of diagnostic features for images from the training set. N – normal, P – pathology, DF – direction field.

Image	DF	Type	K_1	K_2	K_3	K_4
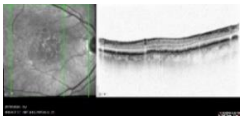		N	2	0.18	0	0.998
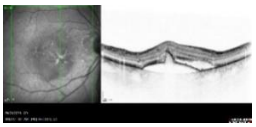		P	455	0.33	15	0.994
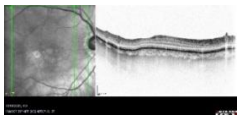		N	3	0.17	1	0.997
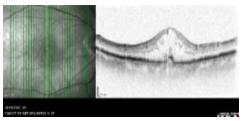		P	540	0.41	32	0.993

For normal images, K1 values range from 0 to 3, indicating the absence of sharp direction changes. K2 ranges from 0.13 to 0.18, reflecting a moderate proportion of regions with a clearly expressed structure. K3 does not exceed 1 (in most cases equals 0), indicating the absence of extensive heterogeneous zones. K4 is close to 0.998, demonstrating high global orderliness of the layers. For pathological images, the feature values differ significantly. K1 increases to 246–540, two to three orders of magnitude higher than in normal cases. K2 increases to 0.27–0.41, which is explained by the appearance of artifact contours and fragmented structures that the weight function interprets as a pronounced direction. K3 takes values from 14 to 32, whereas in normal cases it is close to zero. K4 remains almost unchanged (0.993–0.994), indicating its low

informativeness for class separation. Thus, features K1 and K3 show the strongest difference between normal and pathology. Feature K2 also has diagnostic value, although its interpretation requires caution. Feature K4 does not provide reliable class separation and may be excluded from further analysis.

3.3 Optimization of Method Parameters

To achieve maximum classification accuracy, it is necessary to determine the optimal values of the parameters that affect the construction of the direction field, its filtering, and feature computation. The study was performed on a validation set of 80 images (40 normal, 40 pathology). Accuracy was used as the primary metric. Additionally, F1-score for each class and ROC AUC were evaluated; however, accuracy alone is sufficient for parameter selection, as it correlates well with the other metrics. Three classifiers were compared: Logistic Regression (LR), Decision Tree (DT), and Random Forest (RF). The optimization results for each parameter are presented below.

Mask for the dispersion DF

The size of the mask used for the projection-dispersion computation of the local direction determines the method's sensitivity to fine textures and noise. Small masks (7×7) may lead to excessive detail and false orientations, whereas very large masks (20×20) may cause loss of local features. For each mask size (7×7, 9×9, 13×13, 16×16, 20×20), the accuracy of the three classifiers was calculated. The values are summarized in Figure 5.

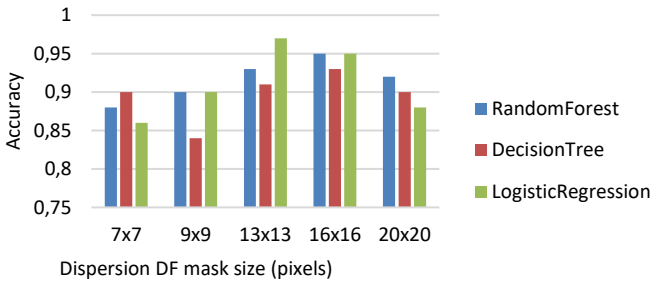

Fig. 5. – Comparison of classifiers by accuracy for different sizes of the dispersion DF mask

The best result (accuracy = 0.97) was achieved by logistic regression with a 13×13 mask. This confirms that for this type of images, the optimal size is 13×13 pixels: it is sufficient to suppress local noise while not smoothing out diagnostically significant gradients. Random Forest shows a gradual increase in accuracy to 0.95 at 16×16, but its maximum value is lower than that of LR. Decision Tree is unstable: at 9×9, accuracy drops to 0.84, indicating its sensitivity to noise. Reducing the mask size to 7×7 worsens the metrics for all models, and increasing to 20×20 also reduces the accuracy of LR and RF due to excessive generalization.

Linear filter mask

After constructing the direction field, linear smoothing filtering is applied in the complex domain. The filter mask size affects the degree of homogeneity of the direction field. Masks of sizes 7×7, 11×11, 13×13, and 17×17 were investigated. The accuracy values for each classifier are shown in Figure 6.

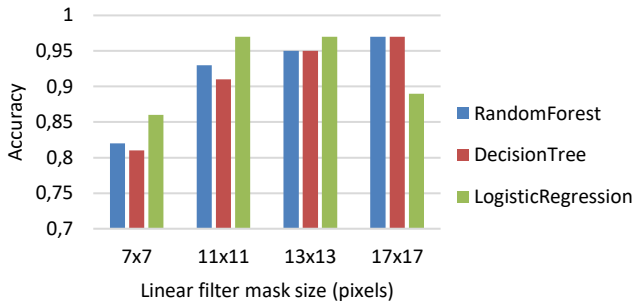

Fig. 6. – Comparison of classifiers by accuracy for different sizes of the linear filter mask

Logistic regression shows maximum accuracy (0.97) already with 11×11 and 13×13 masks, making it the preferred choice. When the mask size is increased to 17×17, LR accuracy drops to 0.89 – apparently due to excessive smoothing that destroys fine structural differences between classes. In contrast, Random Forest and Decision Tree achieve accuracy = 0.97 only at 17×17, indicating their greater tolerance to smoothing, albeit at the cost of using more complex decision rules. With a small 7×7 mask, all models show low accuracy (especially DT – 0.81), confirming the necessity of filtering. Thus, considering the balance between accuracy and robustness, a 13×13 mask in combination with logistic regression is optimal.

Number of filter passes

Linear filtering of the direction field is applied iteratively. The number of passes (mask_pass) determines how strongly the field is smoothed. Small values leave noise, large values may destroy pathological inhomogeneities. The experiment was conducted for numbers of passes from 1 to 90 (step of 10, as well as 1). The accuracy results are presented in Figure 7.

Logistic regression achieves maximum accuracy (0.97) at 30 and 40 passes. When the number of passes exceeds 50, its accuracy drops to 0.91–0.93, which is explained by excessive smoothing: useful pathological contours disappear and the classes become less distinguishable. In contrast, Random Forest and Decision Tree show their best results (accuracy = 0.97) at 60–80 passes, demonstrating high robustness to excessive filtering.

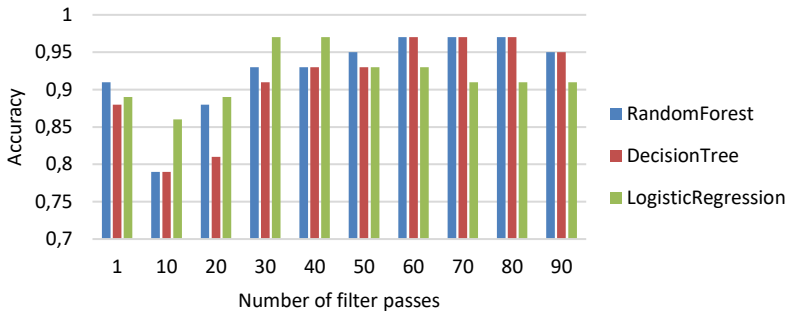

Fig. 7. – Comparison of classifiers by accuracy for different numbers of filter passes

However, with a small number of passes (10), all classifiers sharply lose accuracy (RF and DT drop to 0.79) due to strong noise influence. Considering that logistic regression is simpler to interpret and requires less computational cost, 30–40 passes are optimal for it. For ensemble methods, a larger number of passes can be used, but within the chosen LR model we settle on 30–40 passes.

Threshold value

Feature K2 (relative area of regions with distinct lines) depends on the threshold of the weight function w(x,y), which discards regions with low direction reliability. The threshold range from 0.2 to 0.7 with a step of 0.1 was investigated. The accuracy for the three classifiers is shown in Figure 8. The other features (K1, K3) do not depend on the threshold.

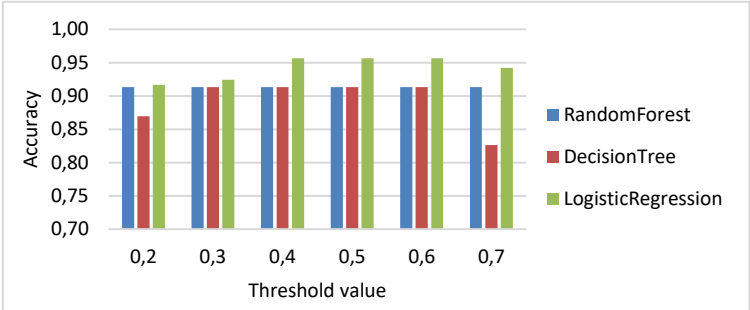

Fig. 8. Comparison of classifiers by accuracy for different threshold values

Logistic regression achieves its highest accuracy (0.96) in the threshold range of 0.4–0.6. At too low a threshold (0.2–0.3), regions with unreliable directions are included in the analysis, reducing accuracy to 0.92. At a threshold of 0.7, some weak but significant structures are lost, and accuracy drops to 0.94. Decision Tree also performs well at thresholds of 0.3–0.6 (accuracy 0.91), but at 0.7 it sharply deteriorates to 0.83, indicating its sensitivity to feature loss. Random Forest maintains a stable accuracy of 0.91

over the entire range, but this value is lower than the optimum for LR. Consequently, a threshold of 0.5 is chosen as the midpoint of the optimal interval for logistic regression.

The conducted comparison shows that logistic regression with properly selected parameters (dispersion DF mask 13×13, linear filter mask 13×13, number of passes 30–40, threshold 0.5) achieves accuracy = 0.97 and ROC AUC = 0.99. It outperforms the decision tree in stability and the random forest in simplicity and computational efficiency, while providing comparable (and for some parameters even higher) accuracy. Decision Tree is unstable when the mask size and threshold are varied. Random Forest yields good results, especially with a large number of filter passes, but does not exceed logistic regression in accuracy under the settings optimal for the latter. Thus, logistic regression is selected as the main classifier for automated detection of type 3 neovascularization biomarkers.

4 Conclusion

In this work, a method for detecting biomarkers of type 3 neovascularization in age-related macular degeneration based on the analysis of retinal OCT images has been developed and experimentally validated. The proposed method includes several sequential steps: construction of the direction field, its smoothing using linear filtering, extraction of three quantitative diagnostic features (density of sharp directional transitions K_1, relative area of regions with distinct lines K_2, number of heterogeneous regions K_3), and subsequent image classification. The fourth considered feature – the degree of layer unidirectionality K_4 – showed low discriminative ability (values in normal and pathological cases are almost identical) and was excluded from the final scheme. The proposed method of analyzing the complex direction field for detecting type 3 MNV biomarkers has not been used before, which defines its scientific novelty.

During the study, the key parameters of the method were optimized: the optimal mask size for direction field construction was found to be 13×13 pixels, the filter mask size 13×13 pixels, the number of filtering passes 30–40, and the weight function threshold 0.5. It was shown that the three selected diagnostic features differ statistically significantly between the normal and pathology classes ($p < 0.001$). A comparative analysis of three classifiers (logistic regression, decision tree, random forest) showed that the best results are achieved using logistic regression: accuracy = 0.97, ROC AUC = 0.99, and F1-score for the pathology class = 0.96.

The developed method has high reproducibility, does not require significant computational resources, and can be integrated into an ophthalmologist's decision support system for automated screening of type 3 neovascularization in AMD. Future research directions include validation of the method on multi-center datasets, its adaptation for the diagnosis of other retinal pathologies (diabetic retinopathy, glaucoma), and the development of a software module for clinical use.

Acknowledgment

The work was carried out within the state assignment of IPSI, NRC "Kurchatov institute".

References

1. Hanson, R.L., et al.: Optical coherence tomography imaging biomarkers associated with neovascular age-related macular degeneration: a systematic review. Eye 37(12), 2438–2453 (2023)
2. Nawash, B., et al.: Prognostic optical coherence tomography biomarkers in neovascular age-related macular degeneration. J. Clin. Med. 12(9), 3049 (2023)
3. Rispoli, M., et al.: Practical guidance for imaging biomarkers in exudative age-related macular degeneration. Surv. Ophthalmol. 68(4), 615–627 (2023)
4. Alex, D., et al.: Subretinal hyperreflective material morphology in neovascular age-related macular degeneration: a case control study. Indian J. Ophthalmol. 69(7), 1862–1866 (2021)
5. Faatz, H., et al.: Vascular analysis of type 1, 2, and 3 macular neovascularization in age-related macular degeneration using swept-source optical coherence tomography angiography shows new insights into differences of pathologic vasculature and may lead to a more personalized understanding. Biomedicines 10(3), 694 (2022)
6. Clemens, C.R., Eter, N., Alten, F.: Current perspectives on type 3 macular neovascularization due to age-related macular degeneration. Ophthalmologica 247(2), 73–84 (2024)
7. Koseoglu, N.D., Grzybowski, A., Liu, T.Y.A.: Deep Learning Applications to Classification and Detection of Age-Related Macular Degeneration on Optical Coherence Tomography Imaging: A Review. Ophthalmol Ther 12(5), 2347–2359 (2023)
8. Zhang, H., et al.: Retinal OCT image segmentation with deep learning: a review of advances, datasets, and evaluation metrics. Comput. Med. Imaging Graph. 102539 (2025)
9. Asani, B., et al.: Evaluation of OCT biomarker changes in treatment-naive neovascular AMD using a deep semantic segmentation algorithm. Eye 38, 3180–3186 (2024)
10. Borrelli, E., et al.: Deep learning in neovascular age-related macular degeneration. Medicina 60(6), 990 (2024)
11. Neri, G., et al.: Deep learning model for automated classification of macular neovascularization subtypes in AMD. Invest. Ophthalmol. Vis. Sci. 66(9), 55 (2025)
12. Saeidian, J., et al.: Segmentation of choroidal area in optical coherence tomography images using a transfer learning-based conventional neural network: a focus on diabetic retinopathy and a literature review. BMC Med. Imaging 24(1), 281 (2024)
13. Karn, P.K., Abdulla, W.H.: Advancing ocular imaging: a hybrid attention mechanism-based U-Net model for precise segmentation of sub-retinal layers in OCT images. Bioengineering 11(3), 240 (2024)
14. Kugelman, J., et al.: A comparison of deep learning U-Net architectures for posterior segment OCT retinal layer segmentation. Sci. Rep. 12, 14888 (2022)
15. Eckardt, F., et al.: Deep learning-based retinal layer segmentation in optical coherence tomography scans of patients with inherited retinal diseases. Klin. Monatsbl. Augenheilkd. 242(9), 903–911 (2025)
16. Michl, M., et al.: Automated quantification of macular fluid in retinal diseases and their response to anti-VEGF therapy. Br. J. Ophthalmol. 106(1), 113–120 (2022)

17. Ibragimova, R.R., et al.: Algoritm segmentatsii makulyarnykh OKT-izobrazheniy dlya analiza patsiyentov s vozrastnoy makulyarnoy degeneratsiyey [Algorithm for segmentation of macular OCT images for analysis of patients with age-related macular degeneration]. Vestnik RGMU (6), 89–96 (2022) (in Russian)
18. Aksenova, L.E., et al.: Razrabotka i aprobatsiya avtomatizirovannoy sistemy analiza OKT-izobrazheniy setchatki [Development and testing of an automated system for analysis of retinal OCT images]. Doklady RAN. Matematika, informatika, protsessy upravleniya 514(2), 169–176 (2023) (in Russian)
19. Khramov, A.G.: Metody vosstanovleniya interferogramm na EVM [Methods of interferogram restoration using computers]. In: Opticheskaya zapis' i obrabotka informatsii [Optical recording and information processing]. KuAI, Kuybyshev (1988) (in Russian)
20. Yoon, W.T., Lee, S.J., Jeong, J.H., Kim, J.H.: Prediction of fellow eye neovascularization in type 3 macular neovascularization (Retinal angiomatous proliferation) using deep learning. PLoS One 19(10), e0310097 (2024)
21. Sokolova, O.A.: K voprosu o sovershenstvovanii metodiki proizvodstva daktiloskopicheskikh ekspertiz v svyazi s vozmozhnoy fal'sifikatsiyey papillyarnykh uzorov [On improving the methodology of fingerprint examinations in connection with possible falsification of papillary patterns]. Vestnik Moskovskogo universiteta MVD Rossii (2), 125–128 (2017) (in Russian)
22. Chentsova, O.B., Prokofyeva, G.L., Teodor, I.L.: Kristallograficheskiy metod obsledovaniya pri nekotorykh zabolevaniyakh glaz [Crystallographic examination method for some eye diseases]. Moscow (1988) (in Russian)
23. Hozman, J., Kubinec, R., Trnka, J., Varenka, J.: Automatic computer evaluation of blood serum crystallograms. In: Biomedical Engineering & Biotechnology, pp. 424–426. Publishing House of the Czech Technical University, Prague (1995)
24. Ilyasova, N.Yu., Ustinov, A.V., Khramov, A.G.: Metody analiza daktiloskopicheskikh izobrazheniy na osnove polya napravleniy [Methods of fingerprint image analysis based on direction field]. Nauchnoye priborostroyeniye (3), 89–101 (1993) (in Russian)
25. Ilyasova, N.Yu., Ustinov, A.V.: Komp'yuternyy analiz izobrazheniya kristallov slezy [Computer analysis of tear crystal image]. In: Proc. 2nd Int. Conf. "Recognition-95", pp. 248–250. Kursk (1995) (in Russian)
26. Dvoryanova, T.P., Ilyasova, N.Yu., Ustinov, A.V., Khramov, A.G.: Komp'yuternaya sistema analiza diagnosticheskikh kristallogramm [Computer system for analysis of diagnostic crystallograms]. Komp'yuternaya optika (16), 90–96 (1996) (in Russian)
27. Ilyasova, N.Yu., Kupriyanov, A.V., Khramov, A.G.: Informatsionnyye tekhnologii analiza izobrazheniy v zadachakh meditsinskoy diagnostiki [Information technologies for image analysis in medical diagnostics]. Radio i svyaz', Moscow (2012) (in Russian)
28. Vinogradov, I.M. (ed.): Matematicheskaya entsiklopediya [Encyclopedia of mathematics], vol. 3. Sovetskaya entsiklopediya, Moscow (1982) (in Russian)